Astron. Astrophys. 359, 766–776 (2000)

ASTRONOMY AND ASTROPHYSICS

Propagation of shock waves in the solar corona with 2-D loop structures

D. Odstrčil[1] **and M. Karlický**[2]

Astronomical Institute, 251 65 Ondřejov, Czech Republic (odstrcil,karlicky@asu.cas.cz)

Received 3 April 2000 / Accepted 4 May 2000

Abstract. Motivated by recent observations of type II radio bursts, we study propagation of shock waves by the two-dimensional numerical magnetohydrodynamic model. Explosion of a hot plasma is investigated for various ratios of the mass density and magnetic field intensity in a fan of coronal loops. Ducting of shock waves occurs along loop-like structure and ducting of possible radio emission in under-dense coronal loops is expected. This provides an alternative to classical explanation that two distinctly separated type II radio bursts are caused by two different shocks. The presented results support the idea that a single solar flare energy release with a single shock can generate coronal disturbances observed as two separate type II radio bursts.

Key words: Magnetohydrodynamics (MHD) – shock waves – methods: numerical – Sun: corona – Sun: radio radiation

1. Introduction

The study of coronal shocks is not an easy task because the solar atmosphere in which they propagate is far from homogeneous and in situ measurements are lacking (Bougeret 1985). Although traveling shocks compress the coronal plasma, the thinness of the physical structure makes them difficult, if not impossible, to image directly. The existence of coronal shocks is therefore often inferred from their indirect effects. Drifting radio emission, type II bursts, is well-observed effect that marks the passage of shocks through the corona (Wild & Smerd 1972).

However, not all shocks produce radio bursts, presumably because they do not meet local conditions for acceleration of electrons required for the excitation of plasma waves and their conversion to radio waves. Further, the type II emission does not outline the entire shock front, but occurs where the shock wave intersects pre-existing structures (Stewart 1984). Multiple type II events are also observed to arise from a single shock which intersects different coronal structures (Robinson & Sheridan 1982).

It has been thought that type II sources may lie in streamers or in regions where the inferred magnetic topology is open (Wild 1970). Spatial observations by radioheliographs suggest that the radio emission only occurs in discrete regions of the solar corona. Uchida (1974) postulated that such regions would occur where the Alfven speed is low so that an MHD wave can steepen into a shock and dissipate energy there. He suggested that the region near the axis of a helmet streamer structure would be suitable because of the high electron densities and low magnetic filed strengths expected there.

Further, it was found that the path of the shock waves causing type II bursts can deviate remarkably from a direct straight line. For instance, Kai (1969) interpreted one peculiar event as the observational evidence for a reflection of shock waves on magnetic wall. In another case, Smerd (1970) described a behind-limb event and concluded a curved path for the type II burst exciters thus being either refracted or magnetically guided.

Duncan (1979) suggested that meter-wave radio emission propagates from the Sun along under-dense magnetic flux tubes. Fundamental and harmonic radio emissions arise within, and are subsequently ducted along, the same under-dense elements of bundles of magnetic flux tubes. The common apparent source of both emissions is the point of escape of radiation from the wave duct at that frequency. This scenario enables to explain the apparent coincidence of fundamental and harmonic radio sources as well as the great heights of solar meter-wave radio sources. Duncan (1979) also estimated that the ducting of radio waves requires magnetic flux tubes with wall over-density factors of about 3.

Interest to type II radio bursts has been renewed recently due to observations by the Yohkoh, SOHO, and TRACE spacecrafts, the radioheliograph in Nancay, as well as by the larger extent of radio frequencies observed by radiospectrographs (GHz, MHz, kHz). Comparative analysis of multi-wavelength observations with a possibility to spatially identify radio sources is important not only for investigation of various dynamic phenomena in the solar corona but for radio emission models as well.

Klassen et al. (1999a) investigated the formation of radio emitting shocks above flaring active regions by combined spectral and imaging observations of type II radio events with solar X-ray imaging observations. They confirmed earlier findings that type II bursts are emitted above active region loops seen in soft X-ray images. The alignment of radio waves at successively lower frequencies is often not radial; the lower frequency sources seem to bend away from the active region. Klassen et al.

Send offprint requests to: D. Odstrčil

(1999a) identified two type II spectral features which systematically precede the well known metric type II burst lanes, the "type II precursor" and the "arc pattern". These features suggest that the shock exists before the type II radio bursts.

Klassen et al. (1999b) analyzed branches of a type II burst observed on 9 July 1996 using the soft-X-ray observations from the Yohkoh spacecraft and radio emission observations from the Nancay radioheliograms and the Potsdam and Ondrejov radiospectrographs. They identified that these radio bursts were located at different places and suggested that they were caused by two shocks. As sketched in Fig. 1, the flare energy release starts at low layers in space among loops L, $L2$, and $L3$. Two MHD shocks are assumed to form and generate type II radio bursts at different locations. The first shock was initiated during the flare impulsive phase by primary energy release processes (probably some magnetic field disturbance). This disturbance was propagating upwards guided along adjacent loop structures. It generated the short-lasting type II burst observed at the top of extended loop systems. The second type II burst was observed with some time delay and its radio source was situated in lower heights between the two extended loop systems. The driver of the first type II burst propagates along two adjacent loops with a twofold speed compared with the second one. In higher coronal heights, in the above lying coronal streamer structure, this event was studied by Pick et al. (1998) using the observations from the Nancay radioheliograph and SOHO/LASCO coronagraphs. An excellent spatial association was found between the position and extension of the radio sources and the CME with distinct leading edges.

The July 9, 1996 coronal event has motivated us to investigate propagation of coronal shocks in large-scale magnetic structures, such as arcades and active region loop systems. Our goal is to investigate whether a single source can generate disturbances that can evolve into two separate shocks or separate type II radio sources due to different plasma parameters in different propagation directions. In a positive case, this would provide an alternative to classical explanation that two signatures of shocks are caused by two sources.

In this paper, we use the two-dimensional numerical magnetohydrodynamic (MHD) model to investigate propagation of shocks in the solar corona with two adjacent coronal loops. We use a simple potential field configuration to represent 2-D analogue of coronal loops and the initial configuration is in static equilibrium in the gravitation field. This initial state is disturbed by introduction of a localized hot plasma that expands and generates MHD waves. Propagation of coronal shocks is investigated for different ratios of the mass density and magnetic field intensity.

2. Numerical model

Large-scale dynamic phenomena in the solar corona can be described by a system of MHD equations. These equations enable determination of macroscopic spatial and temporal variations of the plasma and magnetic field caused by various initial and the boundary conditions. A two-dimensional ideal MHD model of

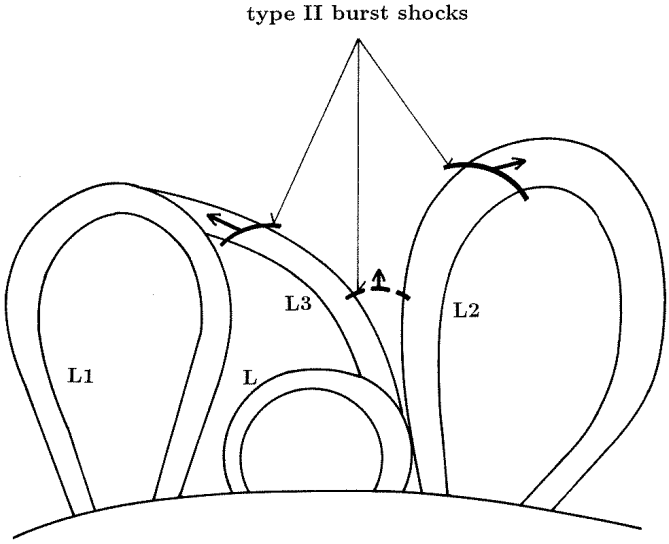

Fig. 1. The interpretation of the July 9, 1996 radio event discussed by Klassen et al. (1999b). The first shock (marked by full-line bows) propagates along loop structure L2 and L3. The second shock (marked by dashed-line bow) propagates between loop structures L2 and L3.

the shock propagation is used in the Cartesian coordinate system. The two independent spatial variables are the horizontal distance, x, and the vertical height, y (y-axis starts in the Sun center). The time-dependent model, written in the conservative form, consists of the following system of equations:

$$\frac{\partial}{\partial t}(\rho) + \frac{\partial}{\partial x}(\rho V_x) + \frac{\partial}{\partial y}(\rho V_y) = 0\,, \tag{1}$$

$$\frac{\partial}{\partial t}(\rho V_x) + \frac{\partial}{\partial x}(\rho V_x^2) + \frac{\partial}{\partial y}(\rho V_x V_y) = - \frac{\partial}{\partial x}(P) + \frac{\partial}{\partial x}\left(\frac{B_x^2}{\mu}\right) + \frac{\partial}{\partial y}\left(\frac{B_x B_y}{\mu}\right)\,, \tag{2}$$

$$\frac{\partial}{\partial t}(\rho V_y) + \frac{\partial}{\partial x}(\rho V_x V_y) + \frac{\partial}{\partial y}(\rho V_y^2) = -\frac{\rho G M_S}{y^2} - \frac{\partial}{\partial y}(P) + \frac{\partial}{\partial x}\left(\frac{B_x B_y}{\mu}\right) + \frac{\partial}{\partial y}\left(\frac{B_y^2}{\mu}\right)\,, \tag{3}$$

$$\frac{\partial}{\partial t}(E) + \frac{\partial}{\partial x}(E V_x) + \frac{\partial}{\partial y}(E V_y) = -\frac{\rho V_y G M_S}{y^2} - \frac{\partial}{\partial x}(P V_x) - \frac{\partial}{\partial y}(P V_y) + \frac{\partial}{\partial x}\left(\frac{B_x}{\mu}(B_x V_x + B_y V_y)\right) + \frac{\partial}{\partial y}\left(\frac{B_y}{\mu}(B_x V_x + B_y V_y)\right)\,, \tag{4}$$

$$\frac{\partial}{\partial t}(B_x) + \frac{\partial}{\partial y}(B_x V_y) = \frac{\partial}{\partial y}(B_y V_x)\,, \tag{5}$$

$$\frac{\partial}{\partial t}(B_y) + \frac{\partial}{\partial x}(B_y V_x) = \frac{\partial}{\partial x}(B_x V_y)\,, \tag{6}$$

where ρ is the mass density, $\boldsymbol{V} = (V_x, V_y)$ is the flow velocity, P is the total pressure (sum of the thermal and magnetic pressures), $\boldsymbol{B} = (B_x, B_y)$ is the magnetic field induction, E is the total energy density (sum of the thermal, kinetic, and magnetic energy densities), and μ is the magnetic permeability. The equation of state is

$$p = R\rho T \ , \tag{7}$$

where R is the gas constant and T is the temperature. The ratio of specific heats, γ = 5/3 is used.

Robust and high-resolution numerical methods are required to simulate propagation of shock waves in plasma with non-homogeneous magnetic field. The explicit finite-difference YD-FCT algorithm (Odstrčil 1993) is used by a space-splitting technique on a non-staggered numerical grid. The algorithm can resolve shocks without needing an artificial diffusion to stabilize the numerical solution (Tóth & Odstrčil 1996). The rectangular computational domain is defined by pairs of boundaries at fixed horizontal positions (left and right) at -0.4 and 0.4 R_S, and at fixed vertical heights (bottom and top) at 1.0 and 1.4 R_S, where R_S = 6.96$\times 10^8$ m is the solar radius. These dimensions roughly corresponds to the observed coronal structures shown in Fig. 1. The computational domain represents a rectangular region with the equidistant difference mesh with 400x200 grid points.

It is not easy to avoid reflections at the boundary without using some special approach, such as a characteristics-based extrapolation. We use a simple technique where all boundaries are assumed to have constant values and they are well away from the interaction region of interest. Two rows of "ghost" cells are used around the computational domain that keep initial values. This boundary condition causes reflection of incident disturbances, however, computational subdomain where the shock propagation is investigated is not affected during the used time period.

3. Initial conditions

In the low corona, within about one solar radius of the solar surface, long-lived magnetically closed structures may be assumed to be in static equilibrium under a balance between the Lorentz force, the plasma pressure gradient, and the gravity force (Priest 1982). Coronal loops are three-dimensional structures, however, we use simplified two-dimensional structures to make understanding of basic mechanisms easier. More complex 3-D scenarios will be incorporated in future work.

We use the coronal arcade model (Oliver et al. 1993) as the first step in specification of the initial conditions. This model assumes that the coronal arcade is in static equilibrium ($\boldsymbol{V}$=0) and the potential magnetic field configuration is given by

$$\begin{aligned} B_x^0 &= B_0 \cos(x/\Lambda) \exp(-y/\Lambda) \ , \\ B_y^0 &= -B_0 \sin(x/\Lambda) \exp(-y/\Lambda) \ , \end{aligned} \tag{8}$$

where Λ (=width/π) is a parameter defining the arcade shape and B^0 is the scaling parameter specified in the next. The width parameter of 0.8 R_S is used in this paper. Note that the total magnetic strength depends only on the vertical height

$$B = \sqrt{B_x^2 + B_y^2} = B_0 \exp(-y/\Lambda) \ . \tag{9}$$

We wish to specify loop-like structures within this coronal arcade model. For this purpose we use the vector potential

$$A^0 = B_0 \cos(x/\Lambda) \exp(-y/\Lambda) \ , \tag{10}$$

that gives the same magnetic field configuration as given by Eq. (8). Thus we have a possibility to superpose any additional vector potential and the resulting magnetic field remains divergence free. The magnetic field components are determined from the following relations

$$\begin{aligned} B_x^0 &= \frac{\partial A}{\partial y} \ , \\ B_y^0 &= -\frac{\partial A}{\partial x} \ . \end{aligned} \tag{11}$$

We assume that loop-like structures have reduced or enhanced intensity of the magnetic field. This can be ensured by modification of the gradient of the vector potential in x-direction within a given spatial region as shown in Fig. 2. The spatial region is specified by two levels of the original vector potential A_L and A_R that correspond to values at X_L = -0.10 and X_R = -0.06 R_S at the height y = 1.1 R_S. The right loop is defined similarly but values are chosen to correspond to values at X_L = 0.06 and X_R = 0.10 R_S. The new gradient of the vector potential between X_L and X_R is chosen such that the derived values of B_y are 2 times smaller or larger then their original values in that region. Note that positions where the vector potential has values of A_L and A_R depends on the height. Thus the loops become wider and curved away from the center as shown by shaded area in Fig. 3 as well as by wider profiles in Fig. 4.

We assume that the coronal plasma is an isothermal and fully ionized gas which satisfies the perfect gas law. The temperature is constant with a value of T_0 = 1.5 MK everywhere including coronal loops. Since the magnetic field is potential and thus force-free, the equilibrium is given by balanced forces of the vertical gradient of the thermal pressure and the gravity forces. The density is determined to from the equilibrium condition

$$\frac{\partial}{\partial x}(R\rho T_0) = \frac{\rho G M_S}{y^2} \ . \tag{12}$$

The density is then adjusted to balance changes in the magnetic field strength across loop-like structures to keep the total pressure constant at the constant height. Figs. 3a–c show cases with the weaker background magnetic field and larger density than cases in Figs. 3d–f. Figs. 3b,c,e,f show cases with loop-like structures that have stronger (weaker) magnetic field and lower (higher) density than the surrounding background values.

Coronal shocks and large amplitude waves are caused by localized dynamic events, e.g., by impulsive phase of solar flares. We assume that a shock is generated by an "explosion" of the hot plasma into much cooler surrounding values. The hot plasma is specified as a cylinder with the temperature T_c = 100 MK and with the radius of 0.02 R_S. This cylinder is centered at x = 0 and y = 1.1 R_S for Cases 0 and 1, and at x=-0.082 and y = 1.1 R_S for Case 2 as shown in Fig. 3.

Six cases are considered in this paper as shown in Fig. 3. These cases differ by the geometry of the magnetic field and

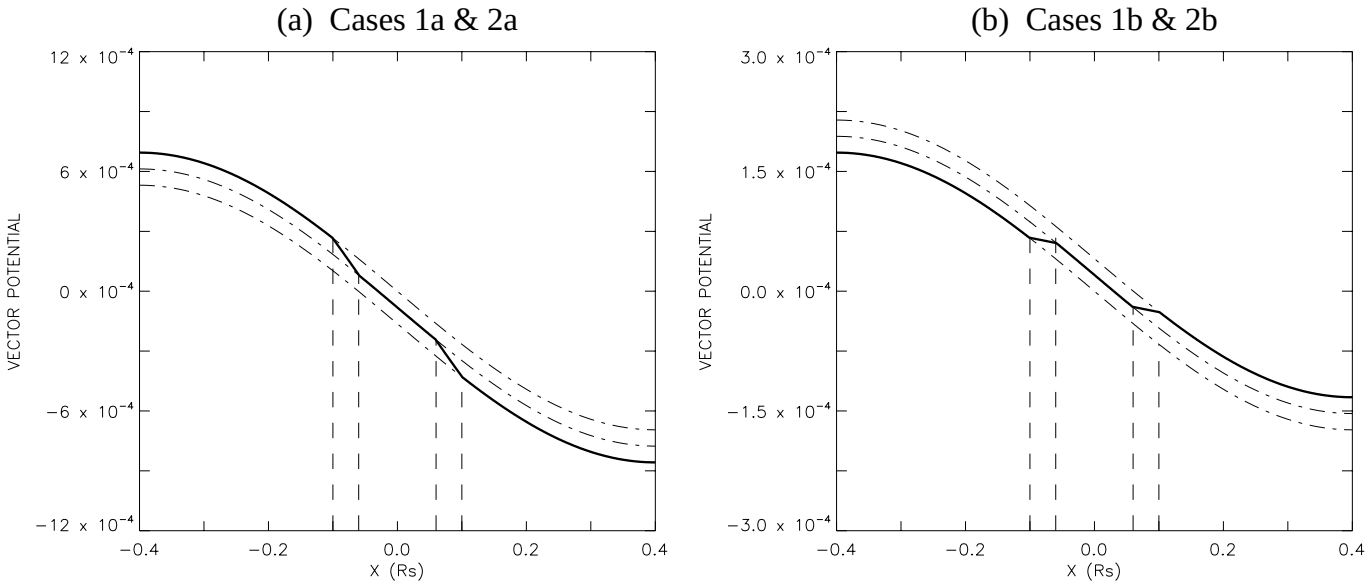

Fig. 2a and b. Specification of the vector potential, A, used to compute the magnetic field with a loop-like structure. Values are shown at the constant height y = 1.1 R_S, i.e., along the x-line marked in Fig. 3. The vector potential decreases exponentially in the y-direction as given by Eq. (10). A loop-like structure is introduced by modification of the vector potential between two pairs of constant values of the original profile. The thick solid (dash-dot) line shows decreasing (increasing) gradient that causes reduction (enhancement) of the magnetic field strength. Details are given in the text.

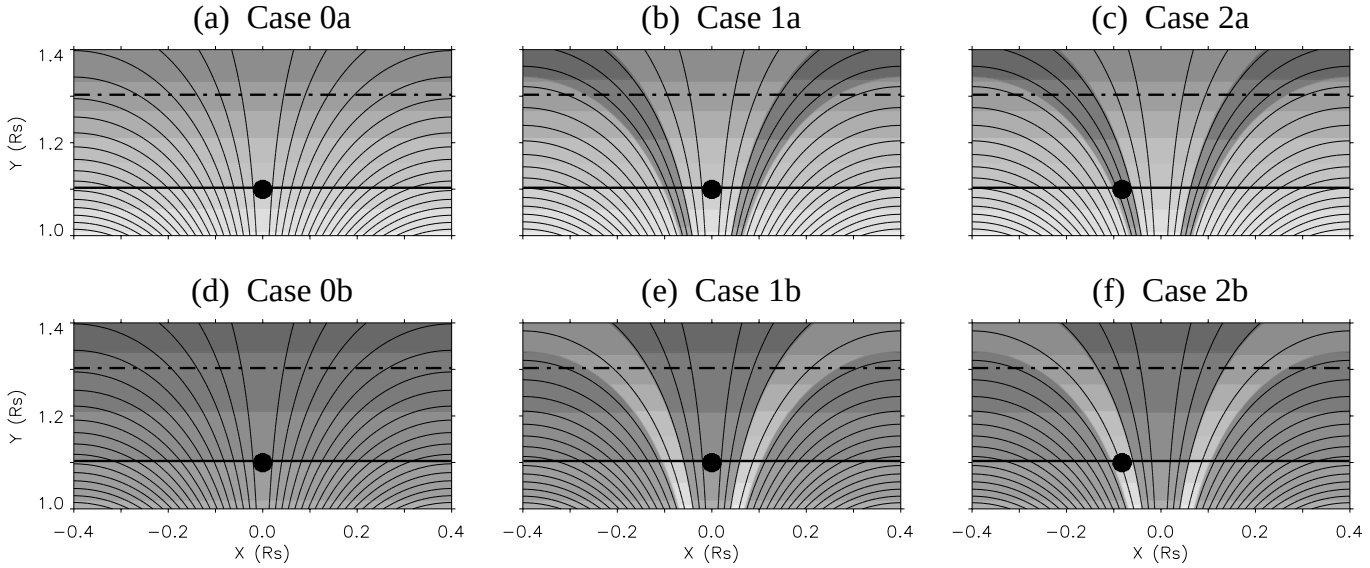

Fig. 3a–f. Six different initial states used for numerical computations in this paper. Solid lines show the magnetic field lines. The shading shows the density distribution (the same logarithmic scale is used for all frames) where the darker color corresponds to larger values. Black area shows hot plasma cylinder with the temperature 100 times higher than the surrounding values. The thick solid and thick dash-dot lines mark two lines at the constant height of y = 1.1 and 1.3 R_S, respectively, along which distribution of parameters is shown in Fig. 4.

position of the explosion site (Fig. 3) and by reduction or enhancement of the magnetic field strength in loop-like structures (Fig. 2). Fig. 4 shows profiles of the total magnetic field, density, and plasma β (ratio of the thermal and magnetic pressures) for different cases at the constant height of 1.1 and 1.3 R_S. Fig. 5 shows maximum and minimum values of these quantities at given heights for all Cases. Maximum values of the magnetic field correspond approximately to the Dulk-McLean model for the heights larger than 1.2 R_S. Minimum values of the magnetic field give the same ratio of the maximum and minimum magnetic pressures for all heights. Maximum values of the number density correspond approximately to the 10x Newkirk model for the heights larger than 1.1 R_S. Minimum values of the number density lie between the 2x and 5x Newkirk model in the heights between 1.1 and 1.3 R_S. These density profiles ensure that the total pressure is constant at a given height. Decreasing

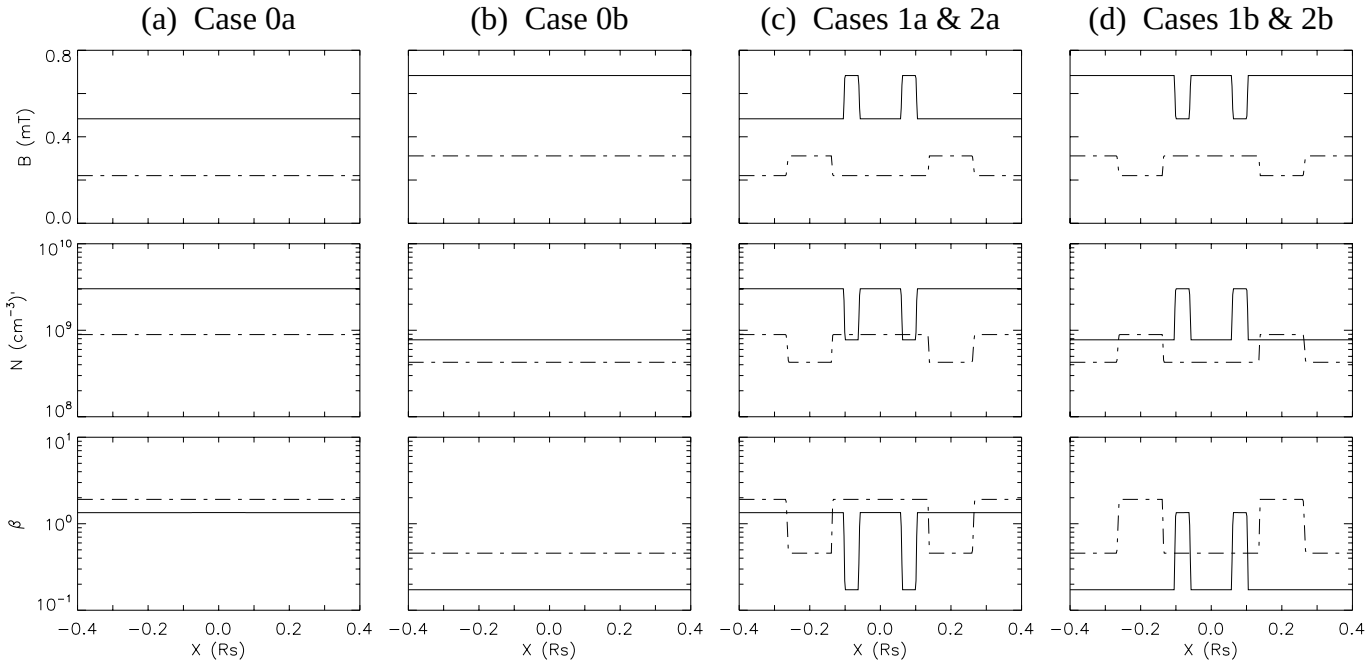

Fig. 4a–d. Profiles of the total magnetic field, number density, and plasma β (ratio of the thermal and magnetic pressures) for Cases 0, 1, and 2. Profiles are shown at the constant heights of 1.1 and 1.3 R_S, along the thick solid and dash-dot lines marked in Fig. 3.

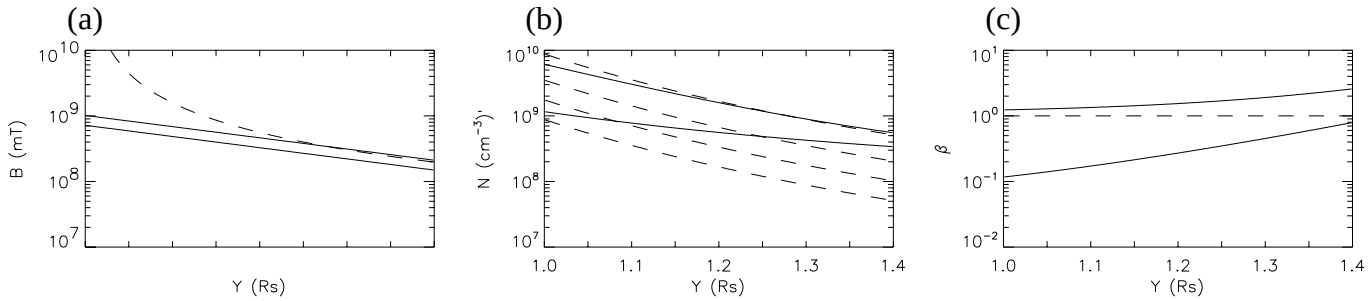

Fig. 5a–c. Maximum and minimum values of the total magnetic field, number density, and plasma β (upper and lower solid lines) at given heights. The total magnetic fields **a** are plotted together with values of the Dulk-McLean model shown by a dashed line. The number densities **b** are plotted together with values of the 1x, 2x, 4x, and 10x Newkirk model shown by four dashed lines. The plasma β values **c** are plotted together with the unity value shown by a dashed line.

ratio between the maximum and minimum density values reflects the decreasing relative importance of the magnetic field strength with the height. The maximum and minimum plasma β values are larger and smaller than unity, respectively.

4. Propagation of a shock wave in homogeneous stratified corona

The Cases 0a and 0b correspond to situations where shocks propagate in homogeneous, vertically stratified corona and disturbed state at different times is shown in Fig. 6. The hot plasma cylinder expands and generates compressive MHD waves that can steepen into MHD shocks. Simple shock structure would result only from point explosion. In our case with a hot cylinder, there are also MHD rarefaction waves that propagates toward the center of the cylinder where they reflect, propagate away from the center, and steepen into secondary weak MHD shocks. Further, note that the field lines are distorted by expanding plasma material, however, the field lines that are "frozen" and that material does not pass through field lines. The MHD waves and shocks are able to propagate across the magnetic field lines.

In the Case 0a, the plasma $\beta > 1$ and only one shock (the fast-mode MHD shock) is formed as shown in Figs. 6a and b. This situation is similar to hydrodynamic shock where the shock front is spherical. The magnetic field lines are deflected away from the shock normal. Large deflections of magnetic field lines occurs in the central region because of the weak strength of the magnetic field does not suppress plasma expansion. This is different from the Case 0b, where the field lines deflected by the fast-mode MHD shock are deflect back by the slow-mode MHD shock. Another difference is that the Case 0b has no significant deflection in the central region because plasma expansion in the strong magnetic field is largely collimated along the field lines.

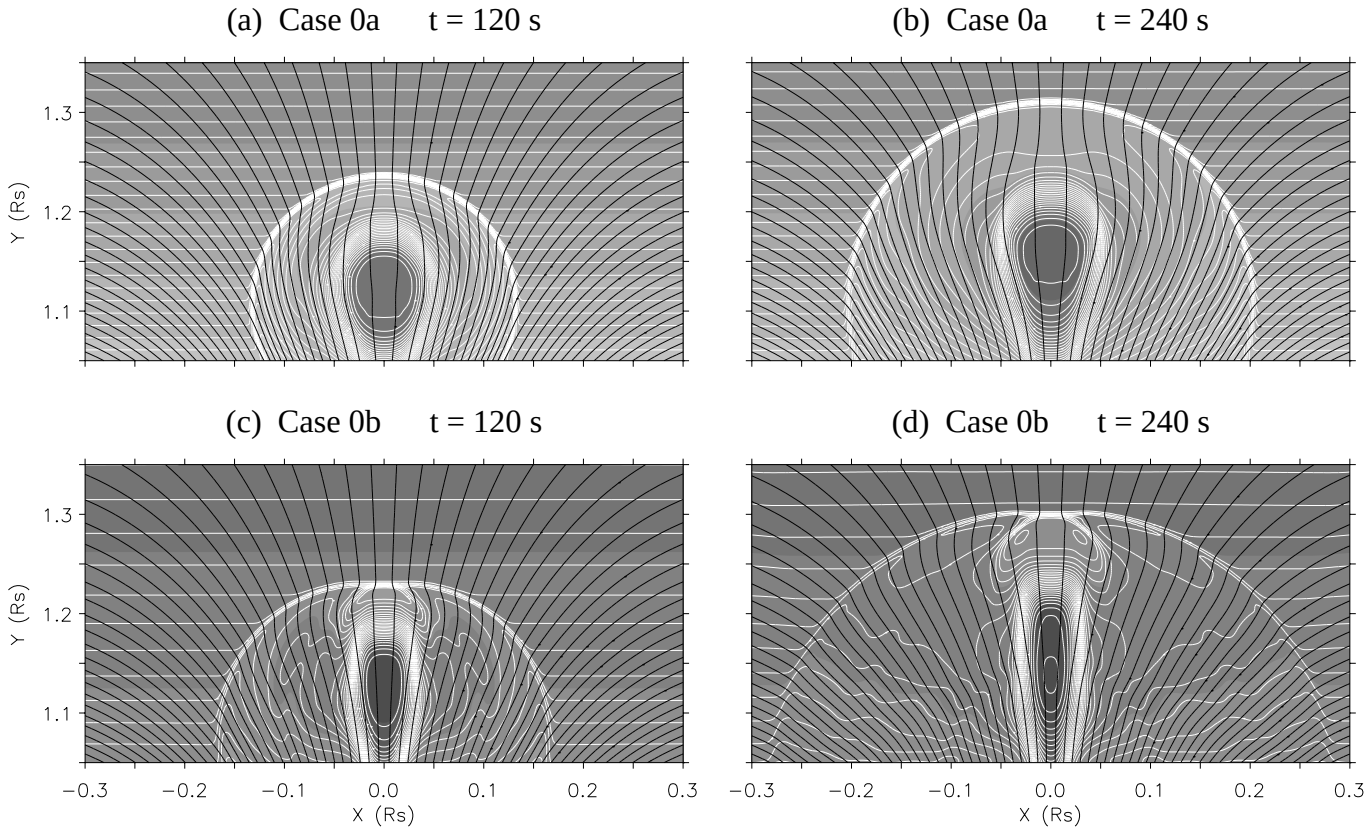

Fig. 6a–d. Disturbed state at t = 120 and 240 s for Cases 0a (top) and 0b (bottom). Density is shown by shading with darker areas corresponding to smaller values. Magnetic field is shown by field lines.

In the Case 0b, the plasma $\beta < 1$ and both fast-mode and slow-mode MHD shocks have formed. The spherical expansion is distorted by the magnetic field and the global structure acquires a non-spherical configuration as shown in Figs. 6c and d. The shock front is horizontally more distant at the height of 1.05 R_S than at 1.1 R_S because of faster propagation in the stronger field. Velocity of MHD waves and shocks depends on the orientation and intensity of the magnetic field. The fast-mode MHD shock is relatively weak and it is the strongest in a direction across the magnetic field lines. The slow-mode MHD shock gives much larger density compression and propagates along the magnetic field lines. The magnetic field lines are bent toward (away from) the front of the fast-mode (slow-mode) shock. There are no fast-mode and slow-mode MHD shocks in perpendicular and parallel directions to magnetic field lines, respectively. Both MHD shocks (or compressive MHD waves) can be observed along the line oblique to magnetic field lines. The fast-mode (slow-mode) MHD shock is more (less) distant from the explosion center and it causes relatively small (large) density compression. The fast-mode MHD shock has large angular extent while the slow-mode MHD waves steep into the shock only near the center and its front is more curved. Note that the shock front has a small dimple in its center. This effect is caused by transition of the fast-mode shock to the slow-mode shock through the intermediate shock. More detail analysis of the fast, intermediate, and slow MHD shocks in the corona, including occurrence of a dimple in the shock front, is given by Steinolfson & Hundhausen (1990) and de Sterck & Poedts (1999).

5. Propagation of a shock wave in structured loop-like corona

The Cases 1a, 1b, 2a and 2b correspond to situations where shocks propagate in structured loop-like corona and disturbed state at different times is shown in Figs. 7 and 8. The hot plasma cylinder expands and generates MHD waves in a similar manner as in the Cases 0a and 0b, but these waves propagate in structured loop-like plasma. The shock propagation is affected by different plasma parameters at different locations and the shock structure acquires more complex configuration.

In the Case 1a, the loop structures have twice stronger magnetic pressure and twice smaller density than the background coronal plasma. The plasma $\beta < 1$ in the loop structures and $\beta > 1$ in the background corona. The hot plasma cylinder is located between loops. The fast-mode MHD shock forms from expanding compressive MHD waves. When this shock reaches coronal loops, it partially reflects and passes through. The Alfven speed is twice larger in the loops than in the surrounding plasma. This causes faster propagation of MHD disturbances in the coronal loops. A shock propagating inside the coronal loop is faster but weaker than in the surrounding background corona. We obtained even faster shock velocities for loops with increased tempera-

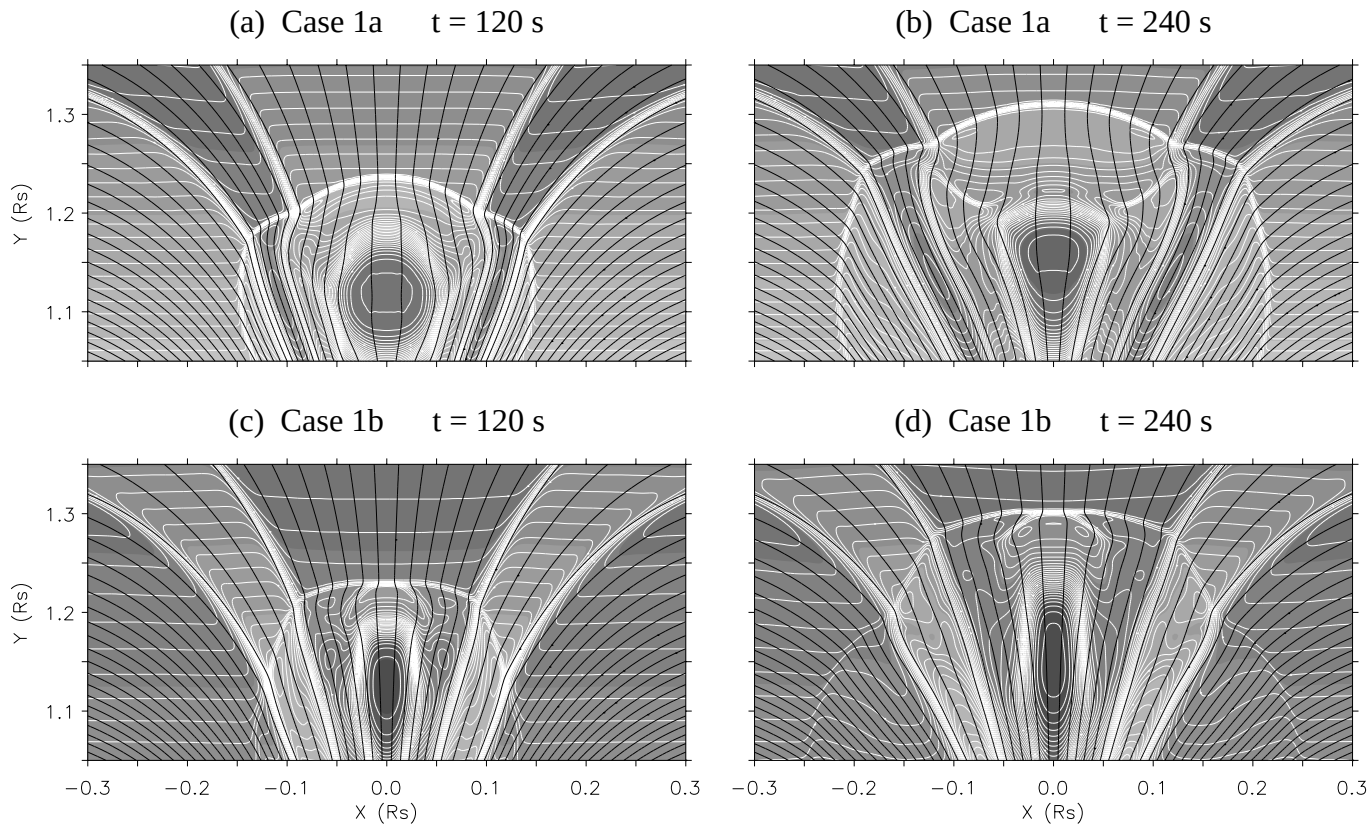

Fig. 7a–d. Disturbed state at t = 120 and 240 s for Cases 1a (top) and 1b (bottom). Density is shown by shading with darker areas corresponding to smaller values. Magnetic field is shown by field lines.

ture where the sound velocity is larger. Some reflected structure forms between the loops and behind the shock. This structure propagates upwardly and does not deflect the magnetic field lines. The expanding plasma in the central region significantly distorts the magnetic field lines. This situation is similar to Case 0a shown in Figs. 6a and b and is possible because of the weak magnetic field. This effect also deflects coronal loops.

In the Case 1b, the loop structures have twice weaker magnetic pressure and twice larger density than the background coronal plasma. The plasma $\beta > 1$ in the loop structures and $\beta < 1$ in the background corona. Both fast-mode and slow-mode MHD shock forms from expanding compressive MHD waves as in the Case 0b. The Alfven speed is twice smaller in the loops than in the surrounding plasma. This causes slower propagation of MHD disturbances in the coronal loops. A shock propagating inside the coronal loop is slower but stronger than in the surrounding background corona.

In the Case 2a, the plasma parameters in the loop structures and in the background corona are the same as in the Case 1a. However, the hot plasma cylinder is located now inside the left loop. Thus the energy released from the explosion is directly converted into the kinetic energy of the shock propagating inside the loop. Therefore the shock propagating inside the coronal loop is significantly faster than in the surrounding background corona. The global shock structure acquires a highly elongated shape. A shock forms also inside the right loop but it is very weak.

In the Case 2b, the plasma parameters in the background coronal plasma and in the loop structures are the same as in the Case 1b. A strong shock forms inside the coronal loop as in the Case 2a. However, this shock propagates slower than in the surrounding background corona. A contact discontinuity can be identifies that separates expanding hot plasma from the original loop plasma. A shock forms also in the right loop but it is more stronger than in the Case 2a. Note that the density is significantly enhanced when the shock passes through the right loop.

6. Tracking of the shock fronts

Two different pieces of the same global shock structure are tracked for different Cases in Figs. 9 and 10. Fig. 9 shows the height where the shock front crosses the vertical line at x = 0 R_s (dash-dot line) and the curved line passing through the center of the left loop (solid line). Fig. 10 shows the local plasma frequencies that correspond to the plasma densities at the shock front heights given in Fig. 9. Assuming that type II radio emission is generated at the local plasma frequency, it is possible to find the shock position from radio observations if the density distribution is known.

In the Case 1a, the shock front reaches the largest height above the explosion site where the released energy is fully converted into the slow-mode MHD shock (Fig. 9a). The shock

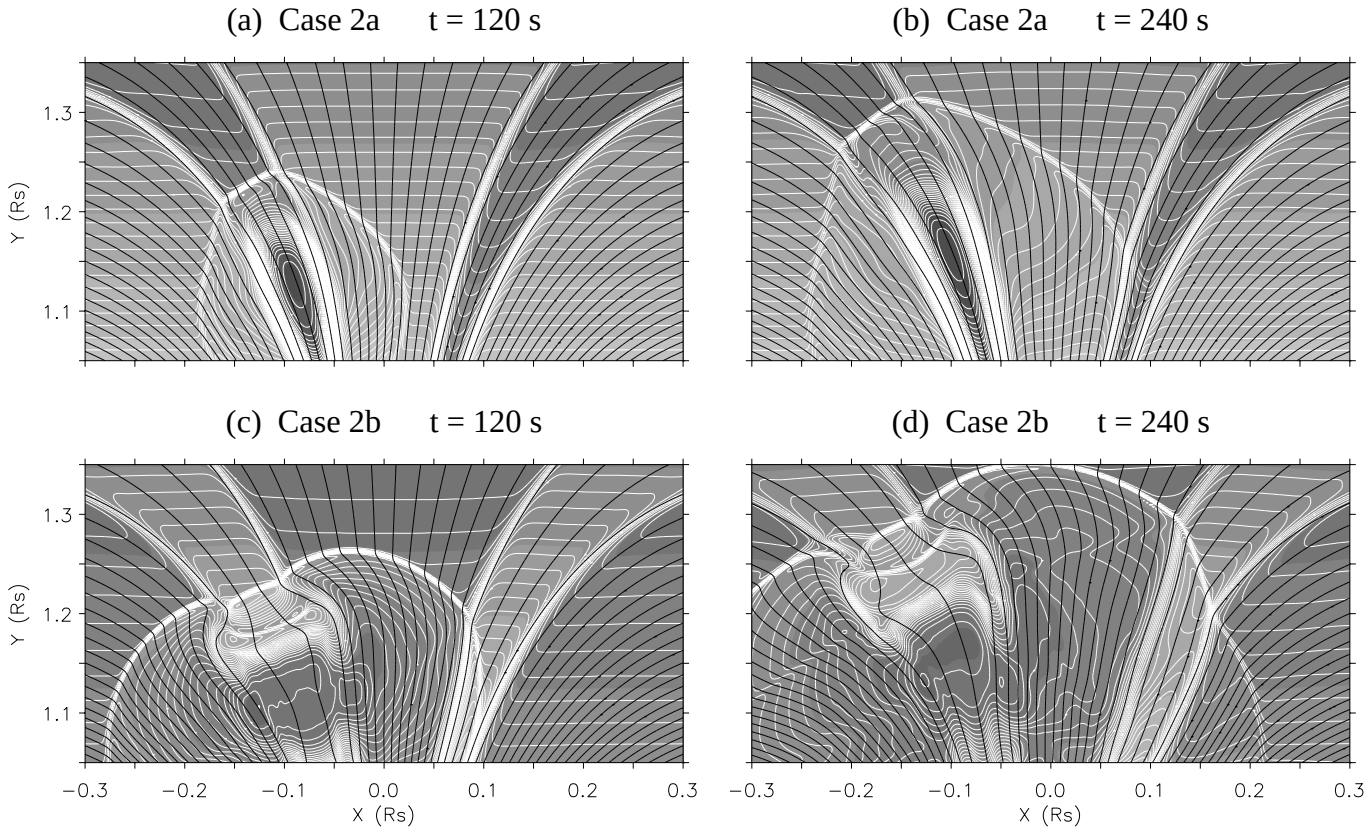

Fig. 8a–d. Disturbed state at t = 120 and 240 s for Cases 2a (top) and 2b (bottom). Density is shown by shading with darker areas corresponding to smaller values. Magnetic field is shown by field lines.

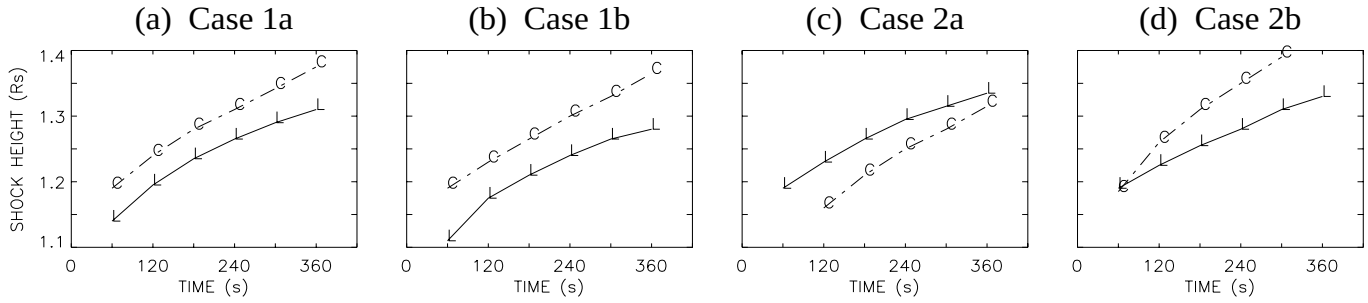

Fig. 9a–d. The vertical height of the shock front reached at different times for different Cases. The dash-dot line with "C" shows the height of the shock front along the vertical line at x = 0 R_S (i.e., in the middle of two loops) in the corona. The solid line with "L" shows the height of the shock front where it crosses the center of the left loop.

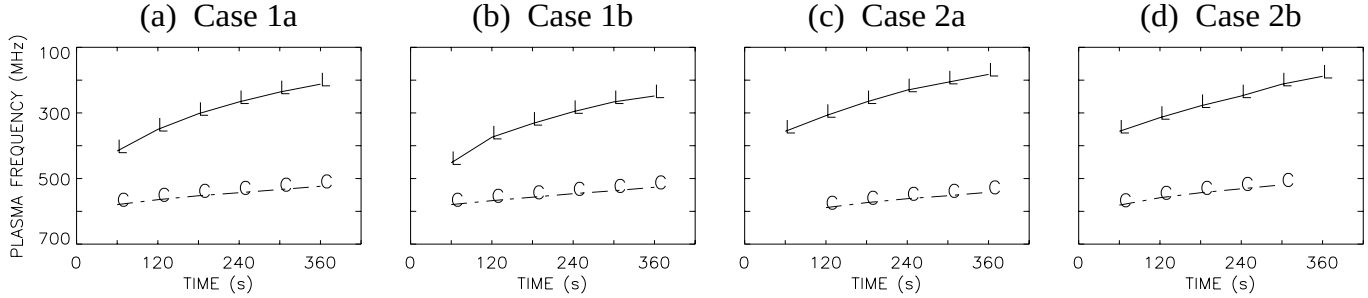

Fig. 10a–d. The local plasma frequency corresponding to the shock front position reached at different times for different Cases. The dash-dot line with "C" shows the plasma frequency along the vertical line at x = 0 R_S (i.e., in the middle of two loops) in the corona. The solid line with "L" shows the plasma frequency where it crosses the center of the left loop. Note that the plasma frequency has reversed scale as is traditionally used by solar radioastronomers.

front in the loop structure reaches comparable distance from the explosion center but its height is smaller. The corresponding Fig. 10a shows that the shock within the loop can generate emission at much lower frequencies than the shock between two loops due to differences in the plasma densities at the shock front.

In the Case 1b, the coronal loops have weaker field and larger densities that causes slower Alfven speed. Both these characteristics causes that the shock propagates slower within the coronal loops (Fig. 9b). The corresponding Fig. 10b shows that the shock within the loop can generate emission at much higher frequencies that the shock between two loops.

In the Case 2a, the shock front in the loops acquires much further distances from the initiation site (Fig. 9c). Energy released from the explosion is directly converted into the shock propagating in the left loop and the shock height is much larger. The corresponding Fig. 10c shows that the shock within the loop can generate emission at much lower frequencies that the shock between two loops.

In the Case 2b, the situation is similar and the explosion energy is released into the left loop. However, the larger characteristic speeds in a region between two coronal loops causes that the shock front reaches here the largest height (Fig. 9d). The corresponding Fig. 10d shows that the shock within the loop can generate emission at much higher frequencies that the shock between two loops.

Note that in all Cases there is only one shock that is tracked along the central vertical line between two loops and along the center of the loop. This is because the magnetic field lines are parallel to the shock propagation at these locations as can be seen in Figs. 7 and 8. Further, note that the shocks propagating in the loop structures are bent away from the vertical direction and thus they show larger "vertical deceleration" than the shocks propagating vertically in the corona between two loops (Fig. 9). Finally, note that the frequency drifts of the radio emission (Fig. 10) depends not only on the shock front velocity (Fig. 9) but also on the vertical gradient of the density in a given coronal structure (Fig. 5).

7. Possible locations of type II radio bursts

For simplicity, we assume that the frequency of radio emission corresponds to the local plasma frequency. Furthermore, we assume that conditions for radio emission are fulfilled in the coronal loops as well as in the space between them. Finally, we assume two observing radio frequencies $f_1 > f_2$ that corresponds to plasma densities $N_1 > N_2$. Fig. 11 schematically shows shock front positions and possible locations of the corresponding sources of type II radio bursts.

Situation with the under-dense loops is shown in Figs. 11a–c. At time t_1 (Fig. 11a) the shock front in the background corona is at the height where a large density corresponds to frequency higher than f_1 that is not observed. However, the shock front crosses the coronal loop with much lower density corresponding to an observable frequency f_1. The radio emission is generated and ducted along the coronal loop and released at the location where the surrounding background density is less than the value N_1 at which the emission was generated. At time t_2 (Fig. 11b) the shock front is at the height where the background density corresponds at the plasma frequency f_1 and the observable radio emission corresponds to the shock front. At the same time, the shock front in the coronal loop is at the position corresponding to the plasma frequency f_2, radio emission is generated, ducted along the coronal loop, and escapes at the site where the surrounding density is less than the plasma frequency at the original position. The situation with the under-dense loops enables radio wave ducting and sites of radio emission can be observed earlier and at much higher positions than at the background corona. At time t_3 (Fig. 11c) the shock front generates the radio emission, at the observable frequency f_2, only in the corona. The radio emission from loops is below f_2.

Situation with the over-dense loops is shown in Figs. 11d–f. At time t_1 (Fig. 11d) the shock front in the background corona is at locations where a density corresponds to observable frequency f_1. However, the shock front crosses the coronal loop with much higher density corresponding to frequency higner than f_1 that cannot be observed. At time t_2 (Fig. 11e) the shock front is at the height where the background density corresponds at the plasma frequency f_2. At the same time, the shock front in the coronal loop is at the position corresponding to the plasma frequency f_1. At time t_3 (Fig. 11f) the shock front generates the radio emission, at the observable frequency f_2, only in the coronal loops. Thus a spatial separation of the radio emission sources occurs also in the case of over-dense loops. However, positions of radio emission sources in the loops trail behind the emission source in the corona between two loops.

8. Conclusion

We have used the two-dimensional ideal MHD model to study the propagation of shocks in the solar corona with coronal loops. A shock is generated by an "explosion" of a hot plasma cylinder and the subsequent evolution of the shock structure is computed for different situations. The parameters of the problem are chosen to specify a situation with moderate shock strength and low plasma β (ratio of thermal to magnetic pressure) that corresponds to conditions in the solar corona. For numerical reasons, the configuration of magnetic field and the flare impulsive processes (as a sudden plasma temperature enhancement) are simplified.

Explosion of hot plasma cylinder in the coronal arcade model with loop structures generates MHD waves. Both the fast-mode and slow-mode MHD shocks form in the low β plasma. The shock propagation is affected by different plasma parameters at different locations and the shock structure acquires complex configuration. The shocks are stronger in the coronal structures with the weaker magnetic field and larger density (lower Alfven velocity) than in the surrounding background plasma. Coronal loops are slightly deflected and the density is enhanced when the shock wave passes through. The density enhancement is more visible for the over-dense coronal loops.

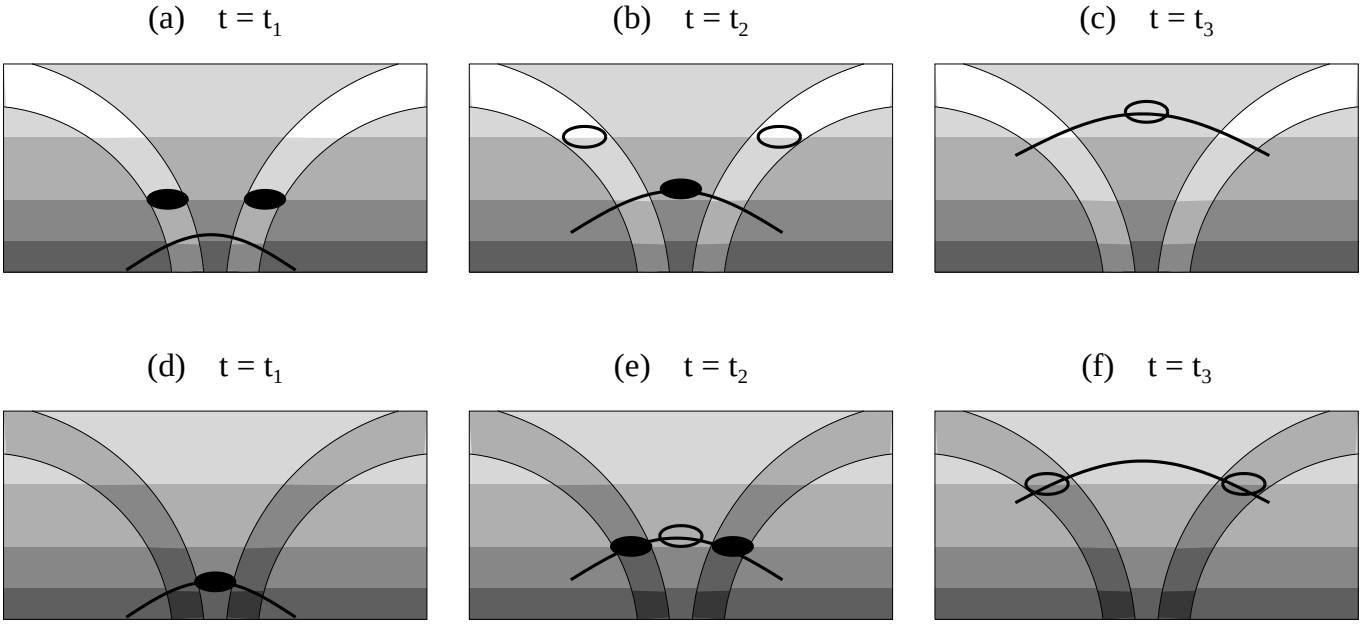

Fig. 11a–f. Schematic illustration of possible locations of type II radio burst sources for shocks propagating in the under-dense (top row) and over-dense (bottom row) coronal loops at three times $t_1 < t_2 < t_3$. One shock propagates in the background corona and the adjacent coronal loops and radio emission is generated at positions with different densities. The shock front is marked by the thick solid line and the site of observed radio emission at the frequency f_1 and f_2 ($f_1 > f_2$) are marked by filled and empty circles, respectively. An alternative explanation of the July 9, 1996 radio event is possible for the scenario with under-dense coronal loops.

Interpretation of type II radio bursts observed on July 9, 1996 provided by Klassen et al. (1999b) and schematically shown in Fig. 1 can have two scenarios. In the the first scenario, suggested by Klassen et al. (1999b) the solar flare generates a shock propagating upward and an electron beam propagating downward in the coronal loop. The particle bombardment transports and deposits the flare energy in deep atmospheric layer and through the evaporation it generates the second shock propagating between the coronal loops. In the second scenario, suggested in this paper, the solar flare generates only one shock that propagates both in the coronal loops and in the surrounding background corona. The shock front generates radio emission at different coronal structures at different frequencies. When the coronal loops structures have lower density, the radio emission can be ducted to higher heights where it can escape. This case can explain the key features of the observed event; the emission source is observed earlier and drifts faster in the coronal loop than in the background corona. Note that when the coronal loop structures have higher density than the surrounding corona, the observed event cannot be explained by this scenario.

The presented results show that the radio spectra, especially at higher frequencies, must be interpreted very carefully. Namely, as evident from the YOHKOH, SOHO, and TRACE observations, the solar atmosphere near active regions is highly structured. with large variations of the magnetic field and temperature. From the equilibrium condition, the variations of the plasma density in coronal loops, separatrices, neutral-line layers, and streamers are expected. Thus, disturbances in the highly inhomogeneous solar atmosphere generate quite naturally (through the plasma emission mechanism) radio bursts in different frequency ranges, although the radio sources are spatially close. Further, superposition of the radio emission in frequency can be also expected. Therefore, the radioheliograph positional measurements in the decimetric frequency range are very desirable.

The presented results have an important implications for space weather forecasting where observations of the metric type II radio bursts have been used to derive initial speed of interplanetary shocks propagating toward the Earth. For flares, like the 9 July 1996 event referenced here, the situation is complex and the forecasting is difficult because: (1) one solar flare can cause occurrence of more distinct sources of the type II radio bursts; (2) propagation of shocks in different coronal structures can be detected with different frequency drifts and different starting times; and (3) coronal shocks that generate metric type II radio burst can be ducted by loop structures and do not propagate into an interplanetary medium. There are also indications that coronal shocks generated by flares (blast waves) can dissipate in the solar corona and only shocks generated and driven by coronal mass ejections can reach the Earth (Gopalswamy et al. 1998).

This work emphasized the effect of various plasma parameters on propagation of coronal shocks. The solar corona is highly inhomogeneous and structured and this property affects propagation of shock waves and locations of possible radio sources. This influence has to be taken into account when interpreting observations of the type II radio bursts. For this purpose, more detailed positional radio observations, comparison with other imaging observations, and 3-D magnetohydrodynamic modeling are necessary.

Acknowledgements. This work was supported by Key Projects K1-003-601 and K1-043-601, and by Grants A3003707 and A3003003 from the Academy of Sciences of the Czech Republic.

References

Bougeret J.-L., 1985, in: Tsurutani B.T., Stone R.G. (eds.), Collisionless Shocks in the Heliosphere: Reviews of Current Research, Geophys. Monogr. Ser., 35, Washington D.C.: AGU, p. 13
de Sterck H., Poedts S., 1999, A&A 343, 641
Duncan R.A., 1979, Solar Phys. 63, 389
Gopalswamy N., Kaiser M.L., Lepping R.P., et al., 1998, J. Geophys. Res. 103, 307
Kai K., 1969, Solar Phys. 10, 460
Klassen A., Aurass H., Klein K.-L., Hoffman A., Mann G., 1999a, A&A 343, 287
Klassen A., Karlický M., Aurass H., Jiřička K., 1999b, Solar Phys. 188, 141
Odstrčil D., 1993, J. Comput. Phys. 108, 218
Oliver R., Ballester J.L., Hood A.W., Priest E.R., 1993, A&A 273, 647
Pick M., Maia D., Kerdraon A., et al., 1998, Solar Phys. 181, 455
Priest R.R., 1982, Solar Magnetohydrodynamics, Dordrecht: Reidel
Robinson R.D., Sheridan K.V., 1982, Proc. Astron. Soc. Australia 4, 392
Smerd S.F., 1970, Proc. Astron. Soc. Australia 1, 305
Steinolfson R.S., Hundhausen A.J., 1990, J. Geophys. Res. 95, 6389
Stewart R.T., 1984, Solar Phys. 94, 379
Tóth G., Odstrčil D., 1996, J. Comput. Phys. 128, 82
Uchida Y., 1974, Solar Phys. 39, 431
Wild J.P., 1970, Proc. Astron. Soc. Australia 1, 365
Wild J.P., Smerd S.F., 1972, Annu. Rev. Astron. Astrophys. 10, 159